

## Ellipticities of Galaxy Cluster Halos from Halo-Shear-Shear Correlations

ZHENJIE LIU,<sup>1</sup> JUN ZHANG,<sup>1,2</sup> CONG LIU,<sup>1</sup> AND HEKUN LI<sup>3</sup>

<sup>1</sup>*Department of Astronomy, Shanghai Jiao Tong University, Shanghai 200240, China*

<sup>2</sup>*Shanghai Key Laboratory for Particle Physics and Cosmology, Shanghai 200240, China*

<sup>3</sup>*Shanghai Astronomical Observatory, Chinese Academy of Sciences, Shanghai 200030, China*

### ABSTRACT

We report the first detection of the halo ellipticities of galaxy clusters by applying the halo-shear-shear correlations (HSSC), without the necessity of major axis determination. We use the Fourier\_Quad shear catalog based on the Hyper Suprime-Cam Survey and the group catalog from the DESI Legacy Surveys for the measurement of group/cluster lensing and HSSC. Our analysis includes the off-centering effects. We obtain the average projected ellipticity of dark matter halos with mass  $13.5 < \log(M_{GH}/M_{\odot}) < 14.5$  within 1.3 virial radius to be  $0.48^{+0.12}_{-0.19}$ . We divide the sample into two groups based on mass and redshift, and we find that halos with higher mass tend to exhibit increased ellipticity. We also reveal that high-richness halos have larger ellipticities, confirming the physical picture from numerical simulation that high-richness halos have a dynamical youth and more active mass accretion phase.

*Keywords:* weak lensing, halo-shear-shear correlation, dark matter halo, ellipticity

### 1. INTRODUCTION

Dark matter halos are large-scale structures formed by the gravity of dark matter. They originate from tiny density fluctuations in the early universe, which collapse and cluster under the influence of gravity, and then evolve and form through continuous merging and accretion within the cosmic web (Zel'dovich 1970). N-body simulations of dark matter reveal the triaxiality of dark matter halos, influenced by the direction of the last major merger and the accretion process along the filaments (Lau et al. 2021). Over time, this connectivity with the cosmic web weakens, and accretion becomes more isotropic, leading to a more spherical shape of halos (Kasun & Evrard 2005; Allgood et al. 2006; Suto et al. 2016; Cataldi et al. 2023). Particularly in the inner regions, baryonic matter, through processes such as star formation and energy feedback, drives the dark matter halos from triaxial to rounder shapes (Chua et al. 2019). Various simulations also report that higher mass halos tend to be less spherical than lower mass halos (Jing & Suto 2002; Allgood et al. 2006; Despali et al. 2014; Bonamigo et al. 2015), mainly because high-mass halos

form later and are more influenced by the surrounding filamentary structure, resulting in stronger triaxiality. Additionally, different dark matter models can affect the ellipticity of halos. For instance, Self-Interacting Dark Matter (SIDM) due to particle collisions tends to produce rounder halos, especially within the interiors of halos (Peter et al. 2013; Gonzalez et al. 2024).

A common method to measure ellipticity involves the gravitational lensing effect around dark matter halos. When light passes near a halo, it is bent by the halo's gravitational field, resulting in distorted images of galaxies. This distortion, commonly referred to as shear, is primarily aligned in the direction tangential to the mass distribution of the lens (Bartelmann et al. 2001). There have been studies that measure the ellipticity of dark matter halos at the galaxy or cluster scale through strong lensing (Oguri et al. 2012; Limousin et al. 2013; Bruderer et al. 2015; Jauzac et al. 2018), convergence map reconstruction (Oguri et al. 2010), and two-dimensional galaxy-galaxy lensing (van Uitert et al. 2012; Clampitt & Jain 2015; Schrabback et al. 2015; Clampitt & Jain 2016; van Uitert et al. 2017; Shin et al. 2018; Dvornik et al. 2019; Gonzalez et al. 2021; Schrabback et al. 2021). Strong gravitational lensing and convergence field analysis are limited to a small number of massive foreground samples and the inner radial regions. Galaxy-galaxy lensing, which is the cross-correlation be-

tween foreground positions and background shear, can analyze the average properties of a large number of low-mass halos by stacking the samples, especially stacking along the major axis to study their anisotropy. However, the actual major axis orientation of halos is unknown, and it is often assumed that the direction of the brightest cluster galaxy (BCG) or satellite galaxies aligns with the halo. This method faces the issue of misalignment of the major axis (Jauzac et al. 2018; Okabe et al. 2020), which would dilute the signal and result in bias.

Simon et al. (2012) shows that the third-order galaxy-galaxy lensing is sensitive to the ellipticity of dark matter halos and their substructures. Subsequently, Adhikari et al. (2015) proposes the use of halo-shear-shear correlation (HSSC) to measure the projected ellipticity of halos to avoid the biases in ellipticity measurements caused by galaxy-halo misalignments. HSSC is a correlation between the shears of two background galaxies around a halo, which reflects the morphology of the halo. They develop an estimator for the halo ellipticity using a simple model of the projected surface density profile of halos and validate it with simulations. Furthermore, Shirasaki & Yoshida (2018) conduct a detailed study on the effects of substructures, projection effects, and off-centering on HSSC measurements using N-body simulations.

In our work, for the first time, we measure the HSSC of halos in galaxy clusters using the observational shear data. It is mainly for the purpose of constraining the average ellipticity for a large sample of cluster halos. Our analysis includes the off-centering effect. §2 illustrates the theoretical model, including models of HSSC and off-centering effects. The data and the method of measurements are introduced in §3 and §4 respectively. We present our main results in §5, and provide comparison with the results from hydrodynamic simulations for discussions. Finally, we conclude in §6.

## 2. MODEL

### 2.1. Multipole Approximation

Due to the evolutionary history and environmental influences, halos inevitably exhibit anisotropy, such as a tendency to elongate along the direction of matter inflow or the filamentary structures. When considering the anisotropy of halos, their density field can be decomposed into monopole and quadrupole terms. The monopole term represents the average density of the halo, while the quadrupole term captures the deviation from sphericity and describes the shape of the halo. Typically, the ellipticity of halos is deemed to be quite small. Following the derivation in van Uitert et al. (2017), the ellipticity is assumed to be minor, allow-

ing the multipole expansion of the surface density to be succinctly expressed as

$$\Sigma(R) = \Sigma(r, \theta) \cong \Sigma_0(r) + \varepsilon \Sigma_2(r) \cos 2\theta \quad (1)$$

where  $R^2 = r^2 \left( q \cos^2 \theta + \frac{\sin^2 \theta}{q} \right)$ ,  $\theta$  represents the angle between the major axis and background galaxy and  $\Sigma_2 = -r \frac{d\Sigma_0(r)}{dr}$ .  $\varepsilon$  is the projected ellipticity, related to the axis ratio  $q$  by

$$\varepsilon = (1 - q)/(1 + q). \quad (2)$$

Moreover, we can assume that the shear components takes the following form:

$$\begin{aligned} \gamma_t(r, \theta) &= \gamma_{t0}(r) + \varepsilon \gamma_{t2}(r) \cos 2\theta \\ \gamma_{\times}(r, \theta) &= \varepsilon \gamma_{\times 2}(r) \sin 2\theta \end{aligned} \quad (3)$$

When neglecting the orientation of dark matter halos, the second-order terms of  $\gamma_{t/\times}$  will be averaged out, thus the measurement results will revert to the traditional stacked galaxy-galaxy lensing, which includes only the isotropic zero-order components,  $\gamma_{t0}$  for  $\gamma_t$  and 0 for  $\gamma_{\times}$ . The relationship between  $\gamma_{t0}$  and surface density is

$$\Sigma_c \gamma_{t0}(r) = \Delta \Sigma(r) \equiv \bar{\Sigma}_0(< r) - \Sigma_0(r), \quad (4)$$

where  $\bar{\Sigma}_0(< r)$  refers to the average surface density within a radius  $r$ , and we term  $\Delta \Sigma(r)$  the excess surface density (ESD).  $\Sigma_c$  is the comoving critical surface density, defined as

$$\Sigma_c = c^2 D_s / [4\pi G D_l D_{ls} (1 + z_l)^2] \quad (5)$$

Here,  $c$  is the speed of light,  $G$  is the gravitational constant, and  $D_s, D_l$ , and  $D_{ls}$  are the angular diameter distances for the lens, source, and lens-source systems, respectively. We employ the analytic formula of the surface density for the Navarro–Frenk–White (NFW, Navarro et al. (1997)) profile in Yang et al. (2006) to describe the isotropic part of halos, i.e.  $\Sigma_0(r)$ . In the following text, for convenience, we denote  $\Sigma_c \gamma_i$  as  $\Gamma_i$ , so that  $\Delta \Sigma = \Gamma_{t0}$ .

For the second-order terms of shears, by solving the Poisson equation, the formula for the second-order term of  $\gamma_t$  can be derived,

$$\Gamma_{t2}(r) \equiv \Sigma_c \gamma_{t2}(r) = -\frac{6\psi_2(r)}{r^2} - 2\Sigma_0(r) - \Sigma_2(r) \quad (6)$$

$$\Gamma_{\times 2}(r) \equiv \Sigma_c \gamma_{\times 2}(r) = -\frac{6\psi_2(r)}{r^2} - 4\Sigma_0(r) \quad (7)$$

where  $\psi_2$  is the quadrupole component of the lensing potential given by:

$$\psi_2 = -\frac{2}{r^2} \int_0^r r'^3 \Sigma_0(r') dr'. \quad (8)$$

In this way, we can obtain the multipole moments of the shear field by solely employing a spherically symmetric halo density distribution model.

The surface density of an ellipsoidal halo varies with angle, leading to corresponding variations in shear, as shown in Eq.3. Naturally, by correlating shears on different angle around a halo, the effect from the second-order ellipticity-dependent terms emerge, eliminating the need to define the axis direction. Ignoring other factors like off-centering and substructure, we can straightforwardly multiply the tangential shears from varying orientations as follows,

$$\begin{aligned} \zeta_{tt}^{\text{cen}}(r_1, r_2, \beta) &= \langle \Gamma_t(r_1, \theta) \Gamma_t(r_2, \theta + \beta) \rangle_\theta \\ &= \Gamma_{t0}(r_1) \Gamma_{t0}(r_2) + \frac{\varepsilon^2}{2} \Gamma_{t2}(r_1) \Gamma_{t2}(r_2) \cos 2\beta. \end{aligned} \quad (9)$$

where  $\beta$  denotes the angular difference of two background galaxies relative to the center. It is evident that this shear correlation does not depend on the orientation of the major axis, and the amplitude of its angular variation depends on the ellipticity of the halo. Similarly, the cross component also has nonzero correlations with itself or the tangential one as follows:

$$\begin{aligned} \zeta_{\times\times}^{\text{cen}}(r_1, r_2, \beta) &= \frac{\varepsilon^2}{2} \Gamma_{\times 2}(r_1) \Gamma_{\times 2}(r_2) \cos 2\beta \\ \zeta_{t\times}^{\text{cen}}(r_1, r_2, \beta) &= \frac{\varepsilon^2}{2} \Gamma_{t2}(r_1) \Gamma_{\times 2}(r_2) \sin 2\beta \\ &= -\zeta_{\times t}^{\text{cen}}(r_1, r_2, \beta). \end{aligned} \quad (10)$$

## 2.2. Off-centering Model

In practice, inaccuracy in the halo center complicates both the modeling and measurement processes. Here, we discuss two aspects of our off-centering model: 1. the impact on the shear signals; 2. the anisotropy of the distribution of the true halo center with respect to the chosen center.

### 2.2.1. Shear Correction

In lensing measurements, off-centering not only results in the misidentification of background galaxies but also leads to the erroneous rotation direction of shear estimators. Hence, we correct the shears in two phases: adjustment for central deviation and alteration in the shear rotation angle. As depicted in the shear field surrounding a halo in Figure 1, with the major axis on the horizontal. The point  $O$  represents the halo's center, the point  $P$  signifies the incorrectly assumed center, and  $q$  marks the location of a background galaxy. The shear components  $\gamma_{t/\times}^{\text{obs}}$  at  $(r, \theta)$  defined with respect to the point  $P$  are related to the components  $\gamma_i(r_{\text{eff}}, \theta_{\text{eff}})$

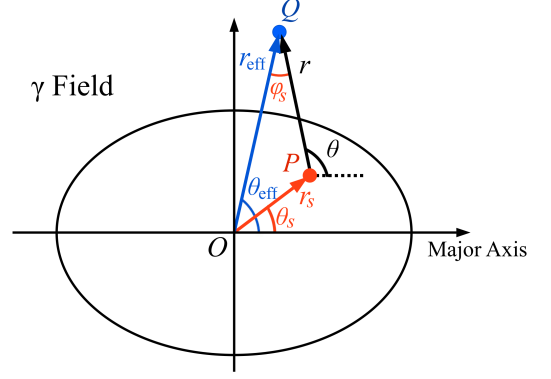


**Figure 1.** Schematic diagram of off-centering. The plane displays the shear field of the halo, where the ellipse represents the dark matter halo, with its major axis aligned along the x-axis, and  $O$  is the halo center set as the coordinate origin.  $P$  is the incorrect halo center, with  $(r_s, \theta_s)$  being its position relative to  $O$ .  $Q$  is the location of the shear measurement, with coordinates  $(r_{\text{eff}}, \theta_{\text{eff}})$  relative to  $O$ . The angle  $\varphi_s$  is between the true halo center and the incorrect center.

centered at point  $O$  via the following form:

$$\begin{bmatrix} \gamma_t^{\text{obs}} \\ \gamma_{\times}^{\text{obs}} \end{bmatrix} = \begin{bmatrix} \cos 2\varphi_s & \sin 2\varphi_s \\ -\sin 2\varphi_s & \cos 2\varphi_s \end{bmatrix} \begin{bmatrix} \gamma_t(r_{\text{eff}}, \theta_{\text{eff}}) \\ \gamma_{\times}(r_{\text{eff}}, \theta_{\text{eff}}) \end{bmatrix} \quad (11)$$

For given values of  $r$ ,  $\theta$ ,  $r_s$ , and  $\theta_s$ , we can solve for  $r_{\text{eff}}$ ,  $\theta_{\text{eff}}$ , and  $\varphi_s$  using the following relations:

$$\begin{aligned} r_{\text{eff}} &= \sqrt{r^2 + r_s^2 + 2r_s r \cos(\theta - \theta_s)}, \\ \cos(\theta_{\text{eff}} - \theta_s) &= \frac{r^2 + r_{\text{eff}}^2 - r_s^2}{2r_s r_{\text{eff}}}, \\ \cos(\varphi_s) &= \frac{r^2 + r_{\text{eff}}^2 - r_s^2}{2r r_{\text{eff}}}, \\ \frac{r}{\sin(\theta_{\text{eff}} - \theta_s)} &= \frac{r_{\text{eff}}}{\sin(\pi - \theta + \theta_s)} = \frac{r_s}{\sin(\varphi_s)}. \end{aligned} \quad (12)$$

### 2.2.2. The Distribution of Off-center

In the monopole model of galaxy-galaxy lensing, we only need to consider the radial distribution of off-centering, and a Rayleigh distribution (Johnston et al. 2007) is considered to be the most realistic,

$$P_r(r_s) = \frac{r_s}{\sigma_s^2} \exp\left(-\frac{r_s^2}{\sigma_s^2}\right), \quad (13)$$

where  $\sigma_s$  describes the dispersion of the center's deviation. However, considering the anisotropic part of halos, the angular distribution of off-centering  $P(r_s, \theta_s)$  could become important, as it exhibits a certain degeneracy with the halo ellipticity. For modeling  $P(r_s, \theta_s)$  of BCGs, we show the distribution of stacked satellite galaxies (red points) and BCGs (contours) from the cluster catalog (described in §3.2) in Figure 2, using the

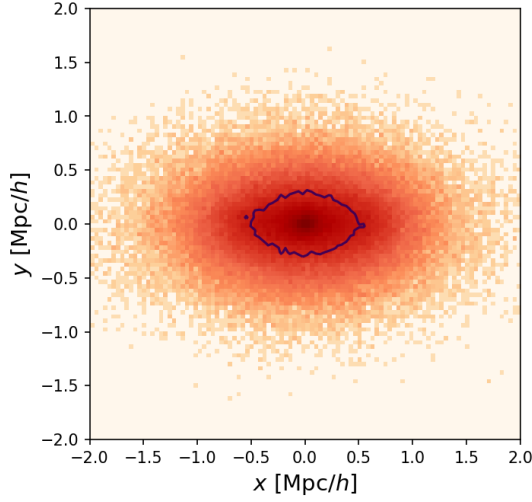


**Figure 2.** The red dots illustrate the distribution of the stacked satellite galaxies, centered around the luminosity-weighted centroid of each cluster and aligned with the long axis. The deep blue contours represent the distribution of BCGs, encompassing about 90% of the BCG positions.

luminosity-weighted centers. The  $x$ -axis represents the major axis direction of the satellite galaxies, and the direction angle  $\phi$  is determined by the quadrupole moments:

$$\tan 2\phi = \frac{2Q_{12}}{Q_{11} - Q_{22}}. \quad (14)$$

$$Q_{ij} = \frac{\sum_k (x_{i,k} x_{j,k} w_k)}{\sum_k w_k}, \quad (15)$$

where  $(x_{i,k}, x_{j,k})$  are the coordinates of the  $k^{\text{th}}$  galaxy in the  $i$  and  $j$  directions relative to the luminosity weighted center, and the weight is  $w_k = 1/(x_{1,k}^2 + x_{2,k}^2)$ . We notice that the angular distribution of the BCGs (contours) is essentially consistent with that of the satellite galaxies (red points), so it can be assumed that the distribution of BCGs relative to the true dark matter halo center has the same projected ellipticity  $\varepsilon$  as the halo. Therefore, we obtain an anisotropic distribution of off-centers by simply transforming the coordinates in Eq.13,

$$P(r_s, \theta_s) = P_r \left( r_s \sqrt{q(\varepsilon) \cos^2(\theta_s) + \sin^2(\theta_s)} / q(\varepsilon) \right) \quad (16)$$

where  $q(\varepsilon)$  is the inverse function of Eq.2. Note that  $q(\varepsilon)$  here represents the anisotropic distribution of off-centers, which could also be set to other values. In §2.2, we discuss the impacts of off-centering model using two extreme cases of off-centering distributions, and find an insignificant effect in ellipticity measurements.

Taking into account the off-centering effect, the ESD can be modeled as

$$\Delta\Sigma^{\text{off}}(r) = \frac{1}{4\pi^2} \int_0^\infty dr_s \int_0^{2\pi} d\theta_s P(r_s, \theta_s) \times \int_0^{2\pi} d\theta \Gamma_t^{\text{obs}}(r, \theta, r_s, \theta_s), \quad (17)$$

and the HSSC model can be formulated as

$$\zeta_{\text{tt}}^{\text{off}}(r_1, r_2, \beta) = \frac{1}{4\pi^2} \int_0^\infty dr_s \int_0^{2\pi} d\theta_s P(r_s, \theta_s) \int_0^{2\pi} d\theta \times \Gamma_t^{\text{obs}}(r_1, \theta, r_s, \theta_s) \Gamma_t^{\text{obs}}(r_2, \theta + \beta, r_s, \theta_s) \quad (18)$$

where  $\Gamma_t^{\text{obs}}$  represents  $\gamma_t^{\text{obs}}$  in Eq.11 multiplied by  $\Sigma_c$ , and  $(r_s, \theta_s)$  is the position of the off-center point. Ultimately, we use the parameter  $f_c$  to depict the proportion of well-centered clusters, so the final ESD and HSSC can be modeled as:

$$\Delta\Sigma(r) = f_c \Delta\Sigma_0(r) + (1 - f_c) \Delta\Sigma^{\text{off}}(r) \quad (19)$$

and

$$\zeta_{\text{tt}}(\beta) = \int_{r_{\min}}^{r_{\max}} dr_1 \int_{r_{\min}}^{r_{\max}} dr_2 P_b(r_1, r_2) \times [f_c \zeta_{\text{tt}}^{\text{cen}}(r_1, r_2, \beta) + (1 - f_c) \zeta_{\text{tt}}^{\text{off}}(r_1, r_2, \beta)]. \quad (20)$$

where  $r_{\min}$  and  $r_{\max}$  respectively refer to the minimum and maximum radii in HSSC measurements, and  $P_b(r_1, r_2)$  is the probability of background galaxies in different radius pairs. Additionally, our theoretical framework necessitates integrating the ESD in Eq.19 and the HSSC in Eq.20 over the mass and redshift distribution of the lens sample to match observed measurements, and they are also weighted by the number of background galaxies.

### 3. DATA

#### 3.1. Shear Catalog

In our analysis, we utilize data from the third public data release of Hyper Suprime-Cam (HSC) Survey (Aihara et al. 2022), which is known for its deep optical observations of the universe, reaching a limiting magnitude of about 26 with excellent spatial resolution. The images have five bands:  $g$ ,  $r$ ,  $i$ ,  $z$ , and  $y$ , with the  $i$  band providing the highest imaging quality. Our shear catalog is processed through the Fourier\_Quad pipeline Liu et al. (2024), covering around 1400 deg<sup>2</sup> and containing about 100 million galaxies. This catalog includes galaxies' basic information such as 3D position, signal-to-noise ratio  $\nu_F$  (Li & Zhang 2021), magnitude, and shear estimates. The Fourier\_Quad shear estimators are derived from the

galaxy power spectrum’s multipole components, comprising five estimators:  $G_1$ ,  $G_2$ ,  $N$ ,  $U$ , and  $V$ , where  $G_i$  resembles the ellipticity components  $e_i$ , and  $N$  serves as a normalization factor,  $U$  and  $V$  are additional correction terms, detailed in Zhang et al. (2017).

To enhance measurement accuracy, we select galaxies with  $\nu_F > 4$ . Photometric redshifts (photo- $z$ ) are obtained using the DEmp method from Nishizawa et al. (2020), also providing their uncertainty estimates  $\sigma_z$ . To mitigate bias from photo- $z$  errors, galaxies with  $\sigma_z > 0.05$  are excluded. In our lensing analysis, we ensure background galaxies had a photo- $z$  greater than the lens redshift by 0.2, i.e.,  $z_s > z_l + 0.2$ , to reduce the dilution of cluster and background galaxies and intrinsic alignment contamination. Based on Liu et al. (2024), using data from multiple bands can improve the signal-to-noise ratio in lensing, hence we chose data from the  $r$ ,  $i$ , and  $z$  bands as our shear samples. Notably, we select galaxy images from different exposures for the HSSC measurement to avoid potential biases due to, e.g., correlated PSF residuals on the same exposure (Lu et al. 2018).

### 3.2. Lens Catalog

Our galaxy cluster catalog is from Yang et al. (2021), which is based on the DESI Image Legacy Surveys DR9. This catalog provides detailed information on the 3D coordinates, richness  $\lambda$ , halo mass  $\log M_G$  and total galaxy luminosity of the clusters. The halo mass estimated using the abundance matching method, ranging from  $10^{11.5} M_\odot/h$  to  $10^{14.5} M_\odot/h$ , with an uncertainty of about 0.2 dex at the high-mass end ( $M_G > 10^{13.5} M_\odot/h$ ) and about 0.45 dex at the low-mass end. In our research, to ensure a high signal-to-noise ratio, we focus on clusters with masses between  $10^{13.5} - 10^{14.5} M_\odot/h$  without richness selection. Additionally, to ensure a sufficient number of background galaxies, we select clusters with  $0.2 < z_l < 0.5$ . Given the relatively small footprint of HSC, we filter our sample to include clusters that overlap with the HSC fields. Ultimately, we identify 23298 lens samples. Notably, while the catalog provides luminosity weighted center of clusters, following Wang et al. (2022), we use the position of the BCG as the center of the galaxy cluster for a more accurate tracking of the halo center in our main analysis.

## 4. MEASUREMENT

In our work, we employ the PDF-symmetrization (PDF-SYM) method to measure the ESD and HSSC signals of galaxy clusters (Zhang et al. 2017; Wang et al. 2022; Liu et al. 2024). This approach is designed to maximize the statistical information from shear estimators

and mitigate statistical biases due to uneven or finite distributions of background sources. The essence of this method involves constructing the probability distribution function (PDF) for the shear signal (or the joint PDF for shear-shear correlations), followed by an optimization process to determine the ideal ESD or HSSC values that achieves a symmetric state of the PDF (or the joint PDF). Here, we provide a detailed introduction to the measurements of ESD and HSSC. Besides, our testing reveals that the quadrupole term of  $\gamma_\times$  is significantly impacted by off-centering effects and shows relatively low sensitivity to ellipticity. Therefore, we rely solely on the results from the  $\gamma_t$  component for parameter constraints. Before the lensing measurements, we test the bias in shear measurements using field distortion and find the biases to be insignificant (see §A).

### 4.1. ESD

In applying the PDF-SYM method, we first stack the tangential shear estimators  $G_t$  of all background galaxies of lens samples into a PDF. Based on Zhang et al. (2017), the unlensed shear estimators  $G_t^S = G_t - g_t(N + U_t)$ , where the  $g_t$  is the real shear of galaxies. The PDF of  $G_t^S$  is assumed to be symmetric with respect to 0, since background galaxies should be randomly oriented. Therefore, by varying the value of  $\hat{\Gamma}_t$ , we could have different PDFs of

$$\begin{aligned} \hat{G}_t &= G_t - \frac{\hat{\Gamma}_t}{\Sigma_c} (N + U_t) \\ &= G_t^S + \frac{\Sigma_c g_t - \hat{\Gamma}_t}{\Sigma_c} (N + U_t). \end{aligned} \quad (21)$$

This step is trying to recover  $G_t$  to its unlensed state whose PDF is symmetric. We achieve the most symmetric PDF of  $\hat{G}_t$  by minimizing the  $\chi^2$  (defined in Eq.36 of Zhang et al. (2017)). When stacking background galaxies without considering orientation, the optimal value obtained will be average ESD value of foreground masses in Eq.4. The feasibility and robustness of our method have been demonstrated in Wang et al. (2022), employing the PDF-SYM technique with the shear catalog generated from DECaLS (Zhang et al. 2022) and studying the halo properties and mass function of galaxy clusters (Yang et al. 2021). To mitigate the significant impacts of baryon effects and other small-scale systematics, we set the minimum radius for all tests at  $0.1 r_{\text{vir}}$ , where  $r_{\text{vir}}$  is the virial radius defined from halo mass  $M_G$  in the lens catalog. For the ESD measurements, 8 points were uniformly spaced on a log-scale from  $0.1$  to  $2 r_{\text{vir}}$ . Fitting  $\Delta\Sigma$  allows us to glean more information about off-centering, which helps break the degeneracy with halo ellipticity in HSSC.

**Table 1.** The prior of all fitting parameters in MCMC approach.

Parameter	$\varepsilon$	$\alpha$	$\sigma_s$	$f_c$
Prior	[0,1]	[0.5,1.5]	[0.1,1.5]	[0,1]

#### 4.2. HSSC

Furthermore, Zhang et al. (2017) introduce symmetrizing the joint PDF of shear estimators for measuring shear-shear correlations, and Liu et al. (2024) successfully apply it in cosmological analysis. Here, we apply the two-point statistics PDF-SYM method to measure the correlation between tangential shears around halos. Initially, we calculate the azimuthal angle for each background galaxy with respect to the BCG center, and identify galaxy pairs with an angular separation of  $\beta$ . In our measurements, since pairs separated by  $\beta$  and  $2\pi - \beta$  are duplicates, we uniformly divide  $\beta$  into eight bins from 0 to  $\pi$ . We then stack the shear estimates  $\hat{G}_t$  and  $\hat{G}'_t$  (defined in Eq. 21) for all pairs into the joint PDF  $P(\hat{G}_t, \hat{G}'_t)$ , assuming two sets of  $\hat{\Gamma}_t$  and  $\hat{\Gamma}'_t$  for galaxy pairs in Eq. 21 with a covariance of the estimated value of HSSC  $\widehat{\zeta_{tt}}$ , i.e.,  $\widehat{\zeta_{tt}} = \langle \hat{\Gamma}_t \hat{\Gamma}'_t \rangle$ . As the estimated HSSC is exactly opposite to real HSSC,  $\widehat{\zeta_{tt}} = -\langle \Gamma_t \Gamma'_t \rangle$ ,  $P(\hat{G}_t, \hat{G}'_t)$  becomes symmetrical. For details on how to generate two sets of  $\hat{\Gamma}_t$  and  $\hat{\Gamma}'_t$ , refer to the methods section in Liu et al. (2024).

In two-point statistics, the shape of the observed field can also produce spurious signals, which need to be subtracted. Therefore, in our ESD measurements, we subtract the lensing results around random points at the same scales, in which the number of random points is about 10 times that of lens galaxies. Systematic errors caused by the shape of the field also exist in HSSC measurements. Besides, beyond individual dark matter halos, the universe's large-scale structure includes filaments, sheets, and voids, which also contribute to the shear correlation between two galaxies. To remove the influence of these cosmological correlations and systematics of intrinsic alignment, we subtract the contribution from random points, i.e., random-shear-shear correlations.

#### 4.3. Parameter Fitting

Our analysis incorporates 4 free parameters: halo ellipticity  $\varepsilon$ , halo mass bias  $\alpha$ , well-centered proportion  $f_c$ , and  $\sigma_s$ . The halo mass used is taken from the group catalog, but it is obtained from abundance matching and it could be problematic. We multiply the group mass by a factor  $\alpha$  to represent the deviation in the halo mass, so the measured halo mass is  $M_{180} = \alpha M_G$ . We adopt the

mass-concentration relation from Duffy et al. (2008),

$$c_{200} = 5.71 (M_{200}/2 \times 10^{12} h^{-1})^{-0.084} (1 + z_l)^{-0.47} \quad (22)$$

where  $M_{200}$  and  $c_{200}$  are defined based on a halo that is 200 times the mean matter density. To align with the halo mass definitions in the lens catalog, we used COLOSSUS (Diemer 2018) to convert these values to  $M_{180}$  and  $c_{180}$ . The sky is divided into 100 subregions using the K-means algorithm in Scikit-learn (Pedregosa et al. 2011), with covariance matrix estimated via the Jackknife method and parameters constrained using the MCMC technique (Christensen & Meyer 2000). Due to the degeneracy of the mass parameter  $\alpha$  with other parameters, we use both the ESD and the HSSC data within radius ranges  $0.1 < r/r_{\text{vir}} < 0.5$  and  $0.1 < r/r_{\text{vir}} < 1.3$  to jointly constrain these four parameters, where  $r_{\text{vir}}$  is derived by the group mass  $M_G$  in the catalog.

## 5. RESULTS AND DISCUSSION

In this section, we present results of the measurements and the average ellipticities. We show the analysis of the projected ellipticity for all samples and vary the radial range of HSSC measurements to find changes in ellipticity within different radial regions. We also assess the dependency of ellipticity on properties such as mass, redshift and cluster richness by dividing the samples into two groups in each case.

### 5.1. All Samples

The upper panel of Figure 3 shows the result of ESD, and the lower two panels show the tangential auto-correlated components of HSSC within two radius ranges. In each panel, we include the best-fit theoretical curves. In the middle and lower panel, the minimum radius is fixed at  $0.1r_{\text{vir}}$ , and the maximum radii are chosen to be  $0.5r_{\text{vir}}$  and  $1.3r_{\text{vir}}$  respectively. The average magnitude of HSSC primarily stems from the monopole component, roughly equal to  $(\Delta\Sigma)^2$ , while its amplitude, which varies in a cosine-like manner, contains information on halo ellipticity. Figure 4 provides a graphical representation of the correlation matrix of all the data points in Figure 3, showing a slight positive correlation among the majority of data.

The row labeled "All" in Table 2 displays the parameter constraints for the entire group sample and Figure 5 shows the 68% and 95% CL contour plots. We find that the halo mass provided in the catalog is biased high, thus yielding an  $\alpha$  value less than 1. For the halo ellipticity, we obtain results that are more than  $2\sigma$  away from zero, and the data from the HSSC clearly exhibit the cosine

**Table 2.** The constraints of four parameters at different radius range for different samples.  $\alpha$  describes the bias of halo mass in the group catalog. The two different richness sub-samples have the same redshift and group mass distributions.

Samples	$\log M_G$	$z$	$N_{\text{lens}}$	$\varepsilon$	$\alpha$	$\sigma_s$	$f_c$	$\chi^2/\text{d.o.f.}$
All	[13.5, 14.5]	[0.2, 0.5]	23298	$0.48^{+0.12}_{-0.19}$	$0.84^{+0.04}_{-0.04}$	$0.33^{+0.05}_{-0.04}$	$0.59^{+0.03}_{-0.03}$	1.03
All (inner)				$0.41^{+0.18}_{-0.24}$	$0.87^{+0.05}_{-0.04}$	$0.37^{+0.07}_{-0.05}$	$0.63^{+0.03}_{-0.03}$	1.65
Low $M_h$	[13.5, 14)	[0.2, 0.5]	19905	$0.36^{+0.23}_{-0.23}$	$0.81^{+0.05}_{-0.05}$	$0.33^{+0.07}_{-0.06}$	$0.60^{+0.03}_{-0.04}$	1.66
High $M_h$	[14, 14.5)	[0.2, 0.5]	3393	$0.53^{+0.16}_{-0.23}$	$0.82^{+0.04}_{-0.04}$	$0.22^{+0.05}_{-0.05}$	$0.60^{+0.07}_{-0.09}$	1.01
Low $z$	[13.5, 14.5)	[0.2, 0.3]	5464	$0.45^{+0.16}_{-0.22}$	$0.94^{+0.06}_{-0.05}$	$0.47^{+0.11}_{-0.09}$	$0.60^{+0.03}_{-0.03}$	1.04
High $z$	[13.5, 14.5)	[0.3, 0.5]	17834	$0.46^{+0.18}_{-0.25}$	$0.90^{+0.05}_{-0.05}$	$0.33^{+0.06}_{-0.05}$	$0.57^{+0.03}_{-0.03}$	1.52
Low $\lambda$	[13.5, 14.5)	[0.2, 0.5]	10203	$0.40^{+0.20}_{-0.25}$	$0.75^{+0.05}_{-0.04}$	$0.30^{+0.09}_{-0.06}$	$0.62^{+0.04}_{-0.04}$	1.97
High $\lambda$	[13.5, 14.5)	[0.2, 0.5]	13095	$0.63^{+0.18}_{-0.21}$	$1.02^{+0.07}_{-0.06}$	$0.38^{+0.07}_{-0.10}$	$0.51^{+0.04}_{-0.09}$	1.60

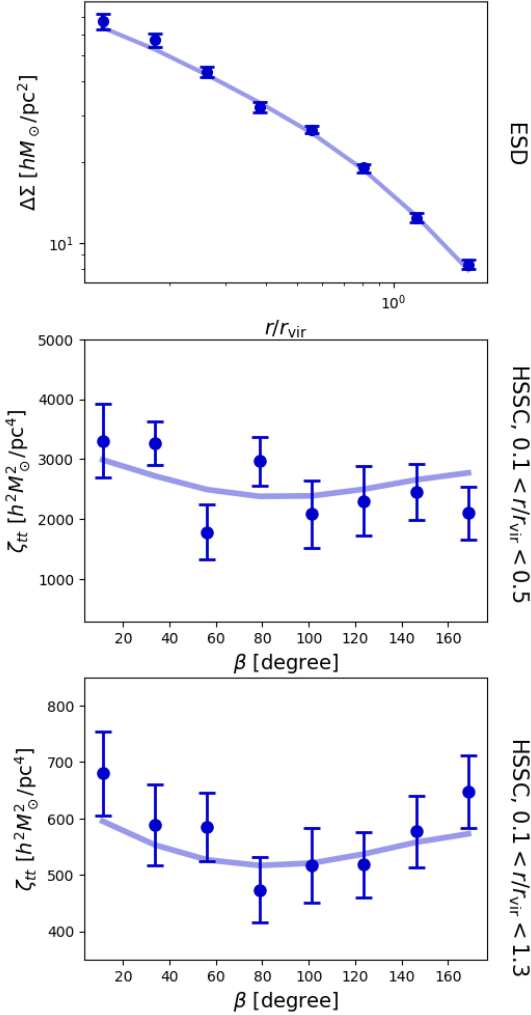


**Figure 3.** The upper panel displays the ESD measurements for all samples, while the middle and the lower panels show the tangential auto-correlated components of HSSC for different maximum radii. The solid lines represent their corresponding best-fit curves.

shape caused by ellipticity, as shown in Figure 3. Fur-

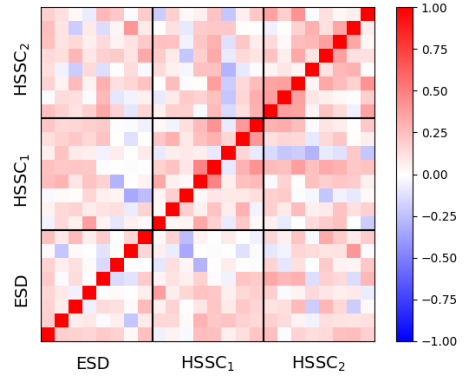


**Figure 4.** Correlation matrix of data points of ESD and HSSC within two different radii for all lens samples. HSSC<sub>1</sub> and HSSC<sub>2</sub> respectively refer to HSSC results within  $0.1 < r_{\text{vir}} < 0.5$  and  $0.1 < r_{\text{vir}} < 1.3$ . The corresponding data points are shown in Figure 3

thermore, we also use the ESD and inner part HSSC, shown in the upper and middle panel of Figure 3, to obtain the ellipticity within inner radius. The results are shown in Table 2 labeled by "All (inner)", which shows a smaller ellipticity in inner halos. This is consistent with conclusions from hydrodynamics simulations, which is commonly linked to baryonic cooling leading to more spherically shaped halos (Springel et al. 2004; Kazantzidis et al. 2004; Cataldi et al. 2023), or possibly to other dark matter models such as SIDM (Peter et al. 2013; Despali et al. 2022).

Besides, we also show two HSSCs involving the cross components for radius within  $0.1 < r/r_{\text{vir}} < 1.3$  in Figure 6. Note that they are not used in constraining the parameters due to their low signal-to-noise ratios. The solid curves are the theoretical predictions using the parameters obtained from ESD and tangential auto-correlated HSSC measurements in Figure 3. We

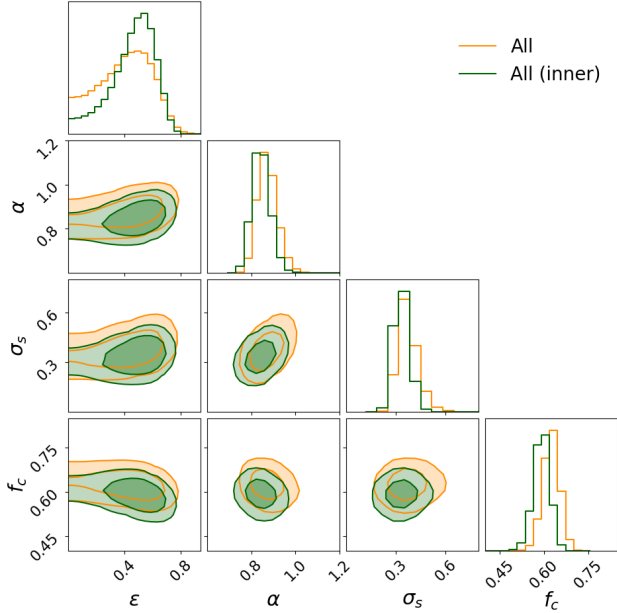


**Figure 5.** The 68% and 95% confidence level contour plots of all lens samples. Green contours are obtained from the results of ESD and HSSC within  $0.1 < r_{\max}/r_{\text{vir}} < 0.5$  and  $0.1 < r_{\max}/r_{\text{vir}} < 1.3$ , whose data points are shown in Figure 3. The results shown in the yellow contours involve only the HSSC within  $0.1 < r_{\max}/r_{\text{vir}} < 0.5$  and the ESD, representing the inner part of halos.

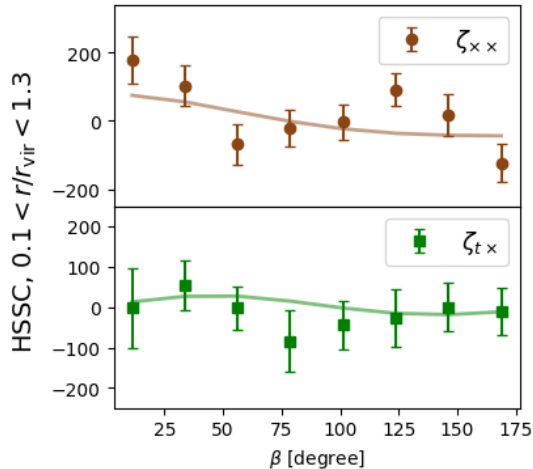


**Figure 6.** HSSC measurements correlated with cross-component within  $0.1 < r/r_{\text{vir}} < 1.3$ . Upper, and lower panels respectively show the results of  $\zeta_{\times \times}$ , and  $\zeta_{t \times}$ . The solid curves are the theoretical predictions using the parameters obtained from data points in Figure 3.

will discuss the utilization of the cross-components in our future work.

In our model, we assume that the anisotropic probability distribution of off-centering anisotropy shares the

same projected ellipticity as the halo, as shown in Eq.16. To examine the robustness of our assumption, we consider two extreme scenarios: one in which the off-center distribution is isotropic ( $q = 1$  in Eq.16), and the other where the BCGs are aligned perfectly along the major axis of the halo ( $q \rightarrow 0$ ). Table 3 presents all constraints for all samples within 1.3 virial radius for these three cases and their corresponding  $\chi^2$  per degree of freedom (d.o.f. = 12). We find that the impact of various off-centering models on the ellipticity results falls within the  $1\sigma$  range, and their  $\chi^2$  are similar.

### 5.2. Dependence on Mass and Redshift

We divide the samples into low mass and high mass sub-samples using a halo mass threshold of  $10^{14} M_{\odot}/h$ , and also separate them into low  $z$  and high  $z$  groups based on the lens redshift at 0.3. The number of lenses in each group is recorded in Table 2. The left and central panels of Figure 7 display the ESD and HSSC measurements for the sub-samples of varying masses and redshifts, respectively, while Table 2 details the constraints on their projected ellipticities.

We observe that lenses with higher mass exhibit higher projected ellipticities compared to lower mass lenses across all radius ranges, although all results fall within a  $1\sigma$  consistency range. This could be due to the fact that larger mass halos form later, with ongoing material inflow and mergers at the periphery, making them more elongated. Our findings are consistent with the conclusions of most simulations (Jing & Suto 2002; Allgood et al. 2006; Despali et al. 2014; Bonamigo et al. 2015). For samples at different redshifts, our results show very similar halo ellipticities. This is reasonable, as the redshifts of the two sub-samples are very close on a cosmic timescale, and their masses are almost identical.

### 5.3. Effect of Richness

Shirasaki & Yoshida (2018) suggest that the presence of subhalos could lead to an overestimation of HSSC compared with the results from simulation. Here, we delve deeper into the effect of richness. It is generally assumed that a galaxy is enveloped by a halo or subhalo, allowing us to explore the influence of subhalo richness on measurements and ellipticity through the abundance of galaxy clusters. Since the halo mass in the group catalog is given by abundance matching, there is a strong correlation between the mass and richness  $\lambda$  in the catalog. Thus, we evenly divided clusters into high- and low- $\lambda$  groups within each narrow redshift and mass bin to make that the 2 samples have similar redshift and group mass distributions. Ultimately, we obtain low- $\lambda$  and high- $\lambda$  samples both with an average mass of  $10^{13.7} M_{\odot}/h$ .



**Table 3.** Fitting results for all parameters and corresponding  $\chi^2/\text{d.o.f.}$  under different off-centering models.  $q(\varepsilon)$  refers to the model in Eq.16, assuming the distribution of off-centering share the same ellipticities as halos.  $q = 1$  and  $q \rightarrow 0$  denote isotropic distribution and BCG alignment along the halo’s major axis, respectively.

Eq.16	$\varepsilon(r_{1.3})$	$\alpha$	$\sigma_s$	$f_c$	$\chi^2/\text{d.o.f.}$
$q(\varepsilon)$	$0.48^{+0.12}_{-0.19}$	$0.84^{+0.04}_{-0.04}$	$0.33^{+0.05}_{-0.04}$	$0.59^{+0.03}_{-0.03}$	1.03
$q = 1$	$0.56^{+0.14}_{-0.20}$	$0.81^{+0.03}_{-0.03}$	$0.30^{+0.03}_{-0.03}$	$0.60^{+0.02}_{-0.02}$	0.96
$q \rightarrow 0$	$0.45^{+0.15}_{-0.19}$	$0.83^{+0.04}_{-0.03}$	$0.35^{+0.05}_{-0.04}$	$0.57^{+0.03}_{-0.03}$	1.05

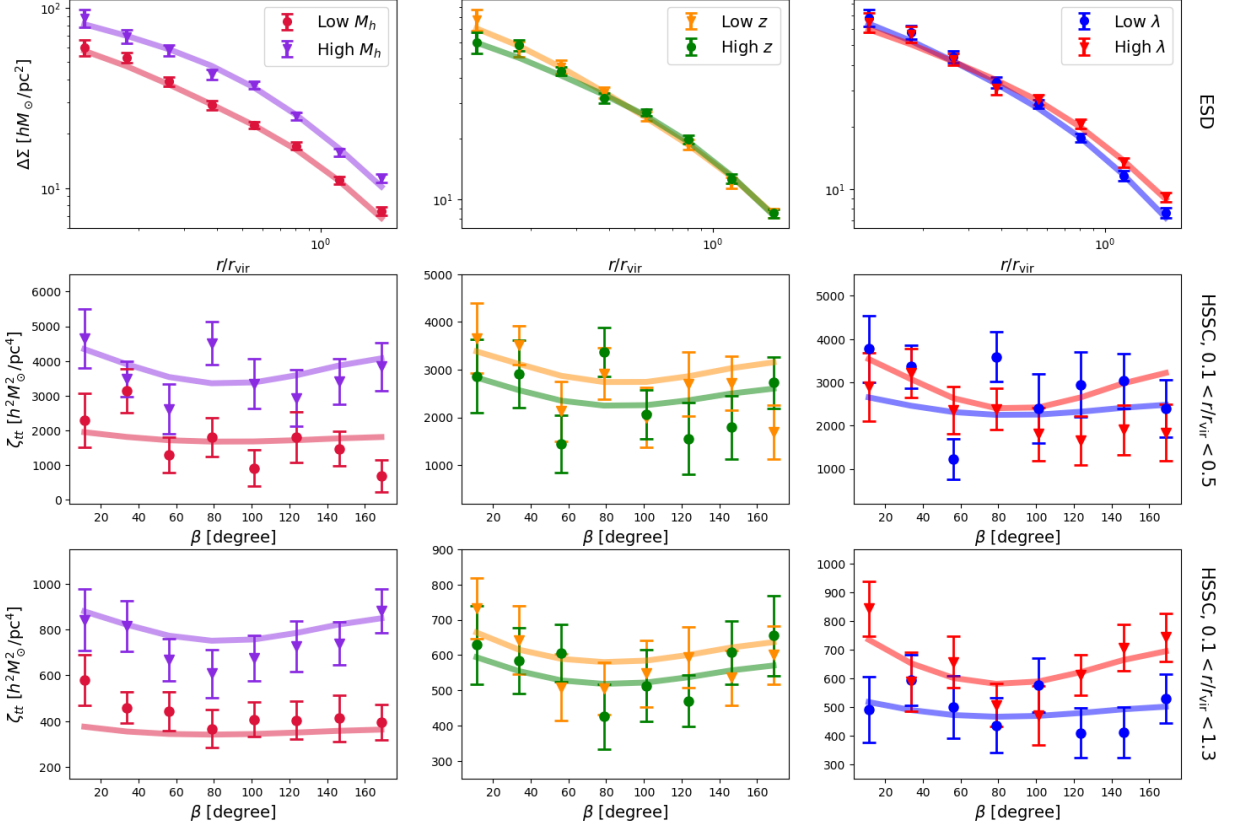


**Figure 7.** The ESD and HSSC measurement results for different subsamples, along with their corresponding best-fit curves. The results in the left, middle, and right panels are derived from lenses of varying masses, redshifts, and richness, respectively.

The right panel of Figure 7 displays the ESDs and HSSCs from halos with different richness. It is evident that the ESDs at small radius are consistent, but in the periphery of high- $\lambda$  lenses is higher than that of low-richness, indicating considerable massive subhalos, which can be described by the off-centering model. Table 2 presents all the constraints of parameters for different samples.  $\alpha$  is highly consistent with 1 for high- $\lambda$  samples, but shows lower halo masses for low- $\lambda$  lenses. For their ellipticity, we find that high- $\lambda$  halos yield larger projected ellipticities, while low- $\lambda$  lenses are more isotropic. Despite taking into account the differences in mass between the two different richness samples, we believe that the difference in their ellipticity also stems from the difference in abundance. In terms

of the environment of halos, those of the similar mass but higher richness are dynamically younger and more prone to incorporating peripheral subhalos during material accretion, resulting in higher ellipticities.

As we define halo richness based on the number of member galaxies in clusters, we evaluate the projected ellipticity of satellite galaxies to check for similar properties. The projected ellipticity of satellite galaxies can be derived from their quadrupole moments, with

$$\varepsilon_1 = \frac{Q_{11} - Q_{22}}{Q_{11} + Q_{22}}, \quad (23)$$

$$\varepsilon_2 = \frac{2Q_{12}}{Q_{11} + Q_{22}} \quad (24)$$

**Table 4.** The ellipticity of dark matter halos at  $z = 0.3$  in the IllustrisTNG simulation. The selection criteria for different samples are consistent with those in lensing measurements in Table 2.

	$\varepsilon_{\text{dm}}$	$\varepsilon_{\text{sat}}$
All	$0.32 \pm 0.17$	$0.29 \pm 0.17$
Low $M_h$	$0.33 \pm 0.19$	$0.31 \pm 0.18$
High $M_h$	$0.27 \pm 0.11$	$0.23 \pm 0.12$
Low $\lambda$	$0.23 \pm 0.11$	$0.21 \pm 0.09$
High $\lambda$	$0.42 \pm 0.20$	$0.38 \pm 0.19$

and

$$\varepsilon_{\text{sat}} = \sqrt{\varepsilon_1^2 + \varepsilon_2^2}. \quad (25)$$

The quadrupole moment is defined in Eq.15 but with the respect to the BCG center. Due to the large uncertainties in ellipticity from the clusters with low richness and the potential for Poisson sampling bias to increase their projected ellipticity, we exclude galaxy clusters with fewer than 20 members from our sample. We find that the ellipticities of low- and high- $\lambda$  groups are very similar,  $0.351 \pm 0.037$  and  $0.353 \pm 0.037$ , diverging from the conclusion of weak lensing measurements. This discrepancy may be attributed to the positional distribution of galaxies not effectively tracing dark matter density, or it could be due to other systematic errors, such as the inclusion of randomly distributed interlopers in the satellite sample, which would reduce the ellipticity (Gonzalez et al. 2021).

#### 5.4. Ellipticity in IllustrisTNG

To deepen our understanding and validate our findings, we calculate the projected ellipticity of halos under similar conditions in the hydrodynamics simulation IllustrisTNG. We utilize the dark matter halo catalog identified by the FOF algorithm for the TNG100-1 simulation of the IllustrisTNG project, assessing their projected ellipticity via the same method applied to satellite galaxies. We identify dark matter halos with mass  $M_{200\text{m}} > 10^{13.5} M_{\odot}/h$  from the snapshot at a redshift of 0.3. We then use the mass weighted center of halos (labeled by "GroupCM" in catalog) and calculate the projected ellipticities of darkmatter and satellite galaxies using Eq.25. We show the outcomes in Table 4. We find that although the projected ellipticity of satellite systems is slightly smaller than that of dark matter halos, they are still very consistent.

We divide the halos into low-mass and high-mass groups based on the threshold of  $M_{200\text{m}} = 10^{14} M_{\odot}/h$ , whose results are presented in Table 4. Surprisingly, the results show that high-mass halos exhibit smaller ellipticities, which contradicts the conclusions from other

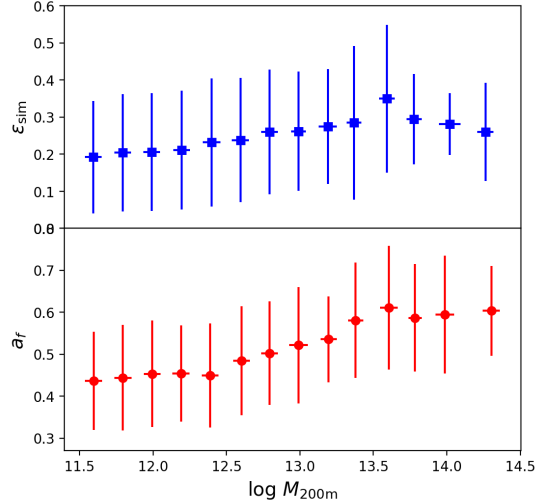


**Figure 8.** The projected ellipticity  $\varepsilon_{\text{sim}}$  of dark matter halos of different masses and their formation times  $a_f$  in the IllustrisTNG simulation.

simulation studies. To further investigate, we expand the mass range of halos to include those with  $M_{200\text{m}} > 10^{11.5} M_{\odot}/h$  for ellipticity calculation and shown them in Figure 8. We observe that the projected ellipticities primarily increased with halo mass in the low and medium mass range, but reversed trend for halos with mass larger than  $10^{13.5} M_{\odot}/h$ . Subsequently, we refer to the halo structure catalog by Anbajagane et al. (2022), examining the relationship between halo formation time and their mass. It is found that, typically, the formation time becomes later as mass increases, but when the halo mass exceeds  $10^{13.5} M_{\odot}/h$ , the formation time remains about  $a_f \sim 0.6$ . This suggests that these massive halos have a similar evolutionary period post-formation, and more massive halos can gather more quickly and weaken their connection to the cosmic web, leading to a more spherical shape.

Finally, we divide halos into low-richness and high-richness groups, ensuring the identical mass and redshift distributions as the same way as we do in the lensing measurements. We find that halos with same mass but higher abundance exhibit larger ellipticities in Table 4, aligning with our measurement outcomes. The formation times  $a_f$  for low- $\lambda$  and high- $\lambda$  halos were calculated to be 0.54 and 0.66, respectively. This suggests that high- $\lambda$  halos form later and are more likely to be in an accretion stage, hence the higher ellipticities. This further validates our explanation for the lensing results. Moreover, this finding is inconsistent with outcomes from the ellipticities of satellite galaxies, suggesting that galaxy clusters may not effectively track the properties of halos in this regard.

## 6. CONCLUSION

Our work is the first to use halo-shear-shear correlations (HSSC) to measure the ellipticity of galaxy cluster halos, avoiding the conventional challenges of determining the major axis in galaxy-galaxy lensing measurements. We consider the off-centering effects in our model of HSSC, which has slight degeneracy with halo ellipticity. We break this degeneracy by jointly constraining the monopole ESD and high-order HSSC, thereby deriving the halo’s projected ellipticity. The galaxy cluster catalog is sourced from DESI, and we select the clusters with halo masses spanning from  $10^{13.5}$  to  $10^{14.5}M_{\odot}/h$  in the redshift range of  $[0.2, 0.5]$ . The shear catalog is derived from the HSC processed by the Fourier\_Quad pipeline, covering an extensive area of  $1400 \text{ deg}^2$  and comprising approximately 100 million galaxies. We employ the PDF-SYM method for measuring ESD and HSSC, which optimizes signal to achieve a symmetric PDF of shear estimators, enhancing statistical information and reducing statistic bias. Additionally, we use the IllustrisTNG simulation to verify our results. Our findings are concluded as follows:

- For all samples, we measure their average projected ellipticity within  $1.3$  varial radius to be  $0.48^{+0.12}_{-0.19}$ . We find that the ellipticity of dark matter halos tends to be larger in the outskirts compared to the inner regions.
- We divide the sample into high- and low-mass subgroups and find that high-mass halos exhibit larger ellipticities. Utilizing dark matter halo catalogs from the IllustrisTNG simulation, it is observed that ellipticities increase with mass in the

low to medium range, but decline for masses above  $10^{13.5}M_{\odot}/h$ . These trends can be ascribed to the formation times of halos.

- We observe that halos at different redshifts show very similar ellipticities.
- We conclude that high-richness halos with same masses exhibit larger ellipticities, indicating that these halos form later and are in a more active stage of mass accretion. This also implies that the richness of a halo can be an indicator of its dynamical age and the extent of its interaction with the cosmic web.

Our research provides valuable insights into the formation and structural evolution of dark matter halos, which is essential for testing and refining cosmological models. Moreover, the methodology established in this work can serve as a foundation for future investigations, encouraging the development of more sophisticated techniques to further unravel the mysteries of halos and cosmos.

**Acknowledgements** Thanks for the valuable suggestions and insightful discussions provided by Wenting Wang, Xiaolin Luo and Zhiwei Shao. This work is supported by the National Key Basic Research and Development Program of China (2023YFA1607800, 2023YFA1607802), the NSFC grants (11621303, 11890691, 12073017), and the science research grants from China Manned Space Project (No. CMS-CSST-2021-A01). The computations in this paper were run on the  $\pi$  2.0 cluster supported by the Center of High Performance Computing at Shanghai Jiaotong University.

## APPENDIX

### A. ONSITE SHEAR BIAS CALIBRATION USING FIELD DISTORTION

Shear biases are typically quantified linearly as:

$$g_i^{\text{obs}} = (1 + m_i)g_i^{\text{true}} + c_i, \quad (\text{A1})$$

in which  $i=1$  or  $2$ , and  $m_i$  and  $c_i$  are the multiplicative and additive biases respectively. Zhang et al. (2019) proposed using the intrinsic distortions of the CCD focal plane (field distortions, FD) to detect  $m$  and  $c$ . FD refers to the image distortion caused by imperfections in the optical system or imaging equipment. These distortions can manifest as twisting, stretching, or compression of the image. This method of calibration uses the properties of the data itself, without the need for simulations or any external datasets. The Fourier\_Quad shear catalog provides two components of FD for each galaxy,  $g_{f1}$  and  $g_{f2}$ . Typically, the average cosmological shear value for all galaxies at the same focal plane position is zero, as they usually cover a large area of the sky. Therefore, by comparing the measured field distortion signals with their true signals in catalog, the biases in shear measurement can be determined.

The FD test results for the shear catalogs of different bands of HSC are presented in Liu et al. (2024). It is however necessary to carry such tests again due to the redshift selection/binning of the background galaxies, as shown in Shen

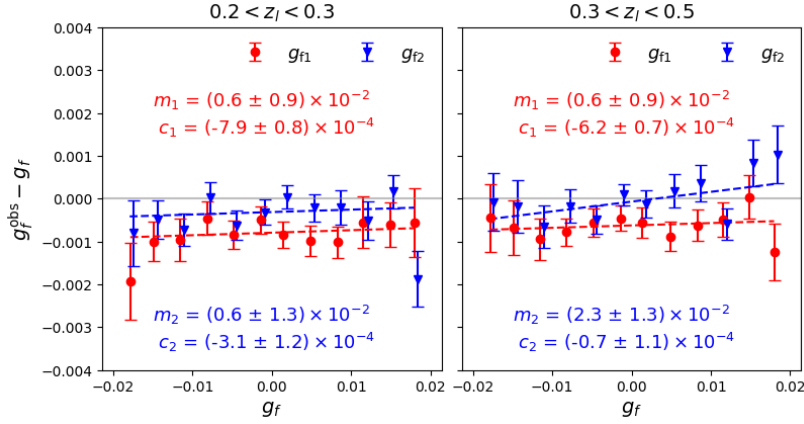


**Figure 9.** The field distortion test for background galaxies of galaxy clusters at two different lens redshift bins. The red and blue data points represent the two shear components  $g_{f1}^{\text{obs}}$  or  $g_{f2}^{\text{obs}}$ . To display them more clearly, the blue points have been horizontally shifted to the right by 0.0005. The dashed lines indicate the fitting lines of Eq. A1, and  $m_i$  and  $c_i$  are their fitting results.

et al. (2024). The resulting shear bias must be caused by selection effects related to the photometric redshift, but the exact physical reason is not clear yet. A convenient feature of the FD test is that one can always carry out such a test for any sub-sample of the shear catalog, which may be subject to selection effects of whatever origin.

We divide all lens galaxy clusters into two subsamples based on redshift in this test. We then find the background galaxies within a radius range of  $0.1-2r_{\text{vir}}$  around the lenses (i.e., all background galaxies measured in the ESD at all radii) and calculate their field distortions. Figure 9 shows the FD results for the two different redshift subsamples. The vertical axis represents the two observed distortion components  $g_{f1}^{\text{obs}}$  (red circles) or  $g_{f2}^{\text{obs}}$  (blue triangles) measured by the PDF method, minus their corresponding true values  $g_f$ . To better approximate reality, each background galaxy is assigned a weight  $\Sigma_c$  defined in Eq.5. If there were no bias in the shear measurement, the observed values should equal the true values, indicated by the gray line in the figures. The dashed lines in figures show the best-fit results of Eq.A1. It is found that most background galaxy samples have a small multiplicative bias, generally at a few percent level. Therefore, we do not apply any corrections to our shear data.

## REFERENCES

- Adhikari, S., Chue, C. Y. R., & Dalal, N. 2015, JCAP, 2015, 009, doi: [10.1088/1475-7516/2015/01/009](https://doi.org/10.1088/1475-7516/2015/01/009)
- Aihara, H., AlSayyad, Y., Ando, M., et al. 2022, PASJ, 74, 247, doi: [10.1093/pasj/psab122](https://doi.org/10.1093/pasj/psab122)
- Allgood, B., Flores, R. A., Primack, J. R., et al. 2006, Monthly Notices of the Royal Astronomical Society, 367, 1781, doi: [10.1111/j.1365-2966.2006.10094.x](https://doi.org/10.1111/j.1365-2966.2006.10094.x)
- Anbajagane, D., Evrard, A. E., & Farahi, A. 2022, MNRAS, 509, 3441, doi: [10.1093/mnras/stab3177](https://doi.org/10.1093/mnras/stab3177)
- Bartelmann, M., King, L. J., & Schneider, P. 2001, A&A, 378, 361, doi: [10.1051/0004-6361:20011199](https://doi.org/10.1051/0004-6361:20011199)
- Bonamigo, M., Despali, G., Limousin, M., et al. 2015, Monthly Notices of the Royal Astronomical Society, 449, 3171, doi: [10.1093/mnras/stv417](https://doi.org/10.1093/mnras/stv417)
- Bruderer, C., Read, J. I., Coles, J. P., et al. 2015, Monthly Notices of the Royal Astronomical Society, 456, 870, doi: [10.1093/mnras/stv2582](https://doi.org/10.1093/mnras/stv2582)
- Cataldi, P., Pedrosa, S. E., Tissera, P. B., et al. 2023, MNRAS, 523, 1919, doi: [10.1093/mnras/stad1601](https://doi.org/10.1093/mnras/stad1601)
- Christensen, N., & Meyer, R. 2000, arXiv e-prints, astro, doi: [10.48550/arXiv.astro-ph/0006401](https://doi.org/10.48550/arXiv.astro-ph/0006401)
- Chua, K. T. E., Pillepich, A., Vogelsberger, M., & Hernquist, L. 2019, MNRAS, 484, 476, doi: [10.1093/mnras/sty3531](https://doi.org/10.1093/mnras/sty3531)
- Clampitt, J., & Jain, B. 2015, arXiv preprint arXiv:1506.03536
- . 2016, Monthly Notices of the Royal Astronomical Society, 457, 4135, doi: [10.1093/mnras/stw254](https://doi.org/10.1093/mnras/stw254)
- Despali, G., Giocoli, C., & Tormen, G. 2014, Monthly Notices of the Royal Astronomical Society, 443, 3208, doi: [10.1093/mnras/stu1393](https://doi.org/10.1093/mnras/stu1393)
- Despali, G., Walls, L. G., Vegetti, S., et al. 2022, MNRAS, 516, 4543, doi: [10.1093/mnras/stac2521](https://doi.org/10.1093/mnras/stac2521)
- Diemer, B. 2018, The Astrophysical Journal Supplement Series, 239, 35

- Duffy, A. R., Schaye, J., Kay, S. T., & Dalla Vecchia, C. 2008, *Monthly Notices of the Royal Astronomical Society: Letters*, 390, L64
- Dvornik, A., Zoutendijk, S. L., Hoekstra, H., & Kuijken, K. 2019, *Astronomy & Astrophysics*, 627, A74
- Gonzalez, E. J., Makler, M., Garcia Lambas, D., et al. 2021, *Monthly Notices of the Royal Astronomical Society*, 501, 5239
- Gonzalez, E. J., Rodríguez-Medrano, A., Pereyra, L., & García Lambas, D. 2024, *Monthly Notices of the Royal Astronomical Society*, 528, 3075
- Jauzac, M., Harvey, D., & Massey, R. 2018, *Monthly Notices of the Royal Astronomical Society*, 477, 4046, doi: [10.1093/mnras/sty909](https://doi.org/10.1093/mnras/sty909)
- Jing, Y., & Suto, Y. 2002, *The Astrophysical Journal*, 574, 538
- Johnston, D. E., Sheldon, E. S., Wechsler, R. H., et al. 2007, arXiv e-prints, arXiv:0709.1159, doi: [10.48550/arXiv.0709.1159](https://doi.org/10.48550/arXiv.0709.1159)
- Kasun, S., & Evrard, A. E. 2005, *The Astrophysical Journal*, 629, 781
- Kazantzidis, S., Kravtsov, A. V., Zentner, A. R., et al. 2004, *The Astrophysical Journal*, 611, L73
- Lau, E. T., Hearin, A. P., Nagai, D., & Cappelluti, N. 2021, *MNRAS*, 500, 1029, doi: [10.1093/mnras/staa3313](https://doi.org/10.1093/mnras/staa3313)
- Li, H., & Zhang, J. 2021, *ApJ*, 911, 115, doi: [10.3847/1538-4357/abec6d](https://doi.org/10.3847/1538-4357/abec6d)
- Limousin, M., Morandi, A., Sereno, M., et al. 2013, *Space Science Reviews*, 177, 155
- Liu, C., Zhang, J., Li, H., Vaquero, P. A., & Wang, W. 2024. <https://arxiv.org/abs/2407.00370>
- Liu, Z., Zhang, J., Li, H., Shen, Z., & Liu, C. 2024, *Science China Physics, Mechanics, and Astronomy*, 67, 270413, doi: [10.1007/s11433-024-2379-0](https://doi.org/10.1007/s11433-024-2379-0)
- Lu, T., Zhang, J., Dong, F., et al. 2018, *The Astrophysical Journal*, 858, 122, doi: [10.3847/1538-4357/aabb50](https://doi.org/10.3847/1538-4357/aabb50)
- Navarro, J. F., Frenk, C. S., & White, S. D. 1997, *The Astrophysical Journal*, 490, 493
- Nishizawa, A. J., Hsieh, B.-C., Tanaka, M., & Takata, T. 2020, arXiv e-prints, arXiv:2003.01511, doi: [10.48550/arXiv.2003.01511](https://doi.org/10.48550/arXiv.2003.01511)
- Oguri, M., Bayliss, M. B., Dahle, H., et al. 2012, *Monthly Notices of the Royal Astronomical Society*, 420, 3213
- Oguri, M., Takada, M., Okabe, N., & Smith, G. P. 2010, *Monthly Notices of the Royal Astronomical Society*, 405, 2215, doi: [10.1111/j.1365-2966.2010.16622.x](https://doi.org/10.1111/j.1365-2966.2010.16622.x)
- Okabe, T., Oguri, M., Peirani, S., et al. 2020, *MNRAS*, 496, 2591, doi: [10.1093/mnras/staa1479](https://doi.org/10.1093/mnras/staa1479)
- Pedregosa, F., Varoquaux, G., Gramfort, A., et al. 2011, *Journal of Machine Learning Research*, 12, 2825
- Peter, A. H. G., Rocha, M., Bullock, J. S., & Kaplinghat, M. 2013, *MNRAS*, 430, 105, doi: [10.1093/mnras/sts535](https://doi.org/10.1093/mnras/sts535)
- Schrabback, T., Hilbert, S., Hoekstra, H., et al. 2015, *Monthly Notices of the Royal Astronomical Society*, 454, 1432
- Schrabback, T., Hoekstra, H., Van Waerbeke, L., et al. 2021, *Astronomy & Astrophysics*, 646, A73
- Shen, Z., Zhang, J., Liu, C., et al. 2024, arXiv e-prints, arXiv:2406.17991, doi: [10.48550/arXiv.2406.17991](https://doi.org/10.48550/arXiv.2406.17991)
- Shin, T.-h., Clampitt, J., Jain, B., et al. 2018, *Monthly Notices of the Royal Astronomical Society*, 475, 2421
- Shirasaki, M., & Yoshida, N. 2018, *MNRAS*, 475, 1665, doi: [10.1093/mnras/stx3289](https://doi.org/10.1093/mnras/stx3289)
- Simon, P., Schneider, P., & Kübler, D. 2012, *Astronomy & Astrophysics*, 548, A102
- Springel, V., White, S. D., & Hernquist, L. 2004, in *Symposium-International Astronomical Union*, Vol. 220, Cambridge University Press, 421–429
- Suto, D., Kitayama, T., Nishimichi, T., Sasaki, S., & Suto, Y. 2016, *Publications of the Astronomical Society of Japan*, 68, 97
- van Uitert, E., Hoekstra, H., Schrabback, T., et al. 2012, *Astronomy & Astrophysics*, 545, A71
- van Uitert, E., Hoekstra, H., Joachimi, B., et al. 2017, *Monthly Notices of the Royal Astronomical Society*, 467, 4131, doi: [10.1093/mnras/stx344](https://doi.org/10.1093/mnras/stx344)
- Wang, J., Yang, X., Zhang, J., et al. 2022, *ApJ*, 936, 161, doi: [10.3847/1538-4357/ac8986](https://doi.org/10.3847/1538-4357/ac8986)
- Yang, X., Mo, H. J., van den Bosch, F. C., et al. 2006, *MNRAS*, 373, 1159, doi: [10.1111/j.1365-2966.2006.11091.x](https://doi.org/10.1111/j.1365-2966.2006.11091.x)
- Yang, X., Xu, H., He, M., et al. 2021, *The Astrophysical Journal*, 909, 143
- Zel'dovich, Y. B. 1970, *A&A*, 5, 84
- Zhang, J., Liu, C., Vaquero, P. A., et al. 2022, *The Astronomical Journal*, 164, 128, doi: [10.3847/1538-3881/ac84d8](https://doi.org/10.3847/1538-3881/ac84d8)
- Zhang, J., Zhang, P., & Luo, W. 2017, *The Astrophysical Journal*, 834, 8, doi: [10.3847/1538-4357/834/1/8](https://doi.org/10.3847/1538-4357/834/1/8)
- Zhang, J., Dong, F., Li, H., et al. 2019, *ApJ*, 875, 48, doi: [10.3847/1538-4357/ab1080](https://doi.org/10.3847/1538-4357/ab1080)